AGU PUBLICATIONS

JGR

Journal of Geophysical Research: Atmospheres

RESEARCH ARTICLE
10.1002/2017JD027221

Key Points:
- CO_2 forcing pattern directly drives atmospheric PET enhancement and oceanic PET weakening
- Feedbacks overall reinforce the forcing effects, particularly with cloud (albedo) feedback enhancing (weakening) atmospheric (oceanic) PET
- Arctic warming amplification, which strongly suppresses atmospheric PET, is found to be sensitive to CO_2 forcing pattern

Supporting Information:
- Supporting Information S1

Correspondence to:
Y. Huang,
yi.huang@mcgill.ca

Citation:
Huang, Y., Y. Xia, and X. Tan (2017), On the pattern of CO_2 radiative forcing and poleward energy transport, *J. Geophys. Res. Atmos.*, *122*, 10,578–10,593, doi:10.1002/2017JD027221.

Received 31 MAY 2017
Accepted 30 JUL 2017
Accepted article online 2 AUG 2017
Published online 19 OCT 2017

On the pattern of CO_2 radiative forcing and poleward energy transport

Yi Huang[1], **Yan Xia**[1], **and Xiaoxiao Tan**[1,2]

[1]Department of Atmospheric and Oceanic Sciences, McGill University, Montreal, Quebec, Canada, [2]Department of Atmospheric and Oceanic Sciences, Peking University, Beijing, China

Abstract A set of general circulation model experiments are conducted to analyze how the poleward energy transport (PET) is related to the spatial pattern of CO_2 radiative forcing. The effects of forcing pattern are affirmed by comparing the conventional doubling CO_2 experiment, in which the forcing pattern is inhomogeneous, to a set of forcing homogenization experiments, in which the top of atmosphere (TOA), surface, or atmospheric forcing distribution is homogenized respectively. In addition, we separate and compare the effects of CO_2 forcing to various feedbacks on atmospheric and oceanic PETs, by using a set of radiative kernels that we have developed for both TOA and surface radiation fluxes. The results here show that both the enhancement of atmospheric PET and weakening of oceanic PET during global warming are directly driven by the meridional gradients of the CO_2 forcing. Interestingly, the overall feedback effect is to reinforce the forcing effect, mainly through the cloud feedback in the case of atmospheric PET and the albedo feedback in the case of the oceanic PET. Contrary to previous studies, we find that the water vapor feedback only has a weak effect on atmospheric PET. The Arctic warming amplification, which strongly affects atmospheric PET, is sensitive to the CO_2 forcing pattern.

1. Introduction

The Earth's climate is shaped by the net top-of-atmosphere (TOA) radiation energy distribution at different latitudes. The solar radiation retained by the Earth exceeds its thermal radiation in the low latitudes, which results in a net radiation surplus; the opposite, i.e., a net radiation deficit, occurs in the high latitudes. This pattern of the net radiation distribution requires energy of other forms to be transported from low to high latitudes. The majority of the needed poleward energy transport (PET) is done mainly by the atmosphere, except in the deep tropics where oceanic transport dominates [e.g., *Trenberth and Caron*, 2001]. In the atmosphere, associated with the energy transport are the atmospheric water and momentum transports which shape the hydrological cycle and general circulation respectively at the planetary scale.

Increase in atmospheric PET is a prominent climatic response during global warming, which is attributable to atmospheric moistening and consequent increase in the transport of atmospheric moist static energy [e.g., *Held and Soden*, 2006; *Hwang and Frierson*, 2010]. Interestingly, atmospheric PET enhancement is accompanied by oceanic PET weakening [*Held and Soden*, 2006; *Huang and Zhang*, 2014], which occurs in line with the Bjerknes compensation hypothesis [*Bjerknes*, 1964] and the slowdown of the meridional overturning circulation [e.g., *Bryden et al*., 2005; *Trossman et al*., 2016].

From an energy budget point of view, changes in PET can be considered to be adjustments that are needed to rebalance the local energy budget while climate reequilibrates during global warming. It is thus of great interest to know how the TOA and surface energy budgets are exactly affected by radiative forcing agents, such as CO_2, as well as by subsequent changes in other climate variables (atmospheric temperature, water vapor, clouds, albedo, etc.), i.e., the climate feedbacks. By analyzing the radiation flux changes in the global warming experiments conducted by general circulation models (GCMs), different authors have investigated and stressed the effects of feedback [e.g., *Zelinka and Hartmann*, 2012] and forcing [e.g., *Huang and Zhang*, 2014], respectively. The recent findings of *Huang et al*. [2016a] point to the importance of forcing distribution, which explains the intermodel difference in the PET changes simulated by the GCMs in the Climate Model Intercomparison Project Phase 5 (CMIP5). The strong correlation between the PET change and forcing pattern suggests that the PET change under global warming may be predicted from the instantaneous forcing, which arguably can be determined with higher certainty than the feedbacks (e.g., that of clouds).

The previous investigations on the PET change during global warming either assumed uniform forcing pattern and thus ignored the forcing inhomogeneity effect [e.g., *Hwang and Frierson*, 2010; *Zelinka and Hartmann*, 2012] or were focused on the TOA radiation budget and thus could not separate the radiative feedback effects on atmospheric and oceanic PETs [e.g., *Zelinka and Hartman*, 2012; *Huang et al*., 2016a]. Hence, critical questions remain unanswered, such as why the atmospheric PET enhances while oceanic PET weakens during global warming and what are the key processes that account for the atmospheric PET enhancement and oceanic PET weakening, respectively? To advance our understanding of the causes of the PET changes, and particularly to ascertain the influence of the CO_2 forcing pattern, we aim at these objectives in this paper: (1) to develop a set of radiative sensitivity kernels of TOA and surface radiation fluxes, from which the patterns of the radiative feedback and their implied atmospheric and oceanic PETs can be inferred respectively, and (2) to conduct a set of GCM experiments in which we compare the PET changes in response to homogenized patterns of CO_2 forcing. In the following sections, we will describe the design of the GCM experiments and analyze the radiative forcing, feedback, and implied PET in order.

2. Method

2.1. GCM Experiments

In this study, we use a coupled atmosphere-ocean GCM, the Community Earth System Model (CESM) version 1.2 of the National Center of Atmospheric Research [*Hurrell et al*., 2013] (model code and documentation available from http://www.cesm.ucar.edu/models/cesm1.2/). The atmospheric component of the model is the Community Atmospheric Model version 5 (CAM5) [*Neale et al*., 2010], configured at 1.9° × 2.5° resolution. The ocean component is the Parallel Ocean Program version 2, which has a total of 60 levels in the vertical with 10 m vertical resolution in the upper 200 m.

We conduct the following experiments using CESM under these different forcing scenarios:

1. CONTROL: in this experiment, the well-mixed greenhouse gases (CO_2, CH_4, N_2O, etc.), ozone, and aerosols are fixed to year-2000 values (Case B_2000_CAM5).
2. CO2x2: the radiative gases are prescribed the same as in CONTROL, except that the atmospheric CO_2 volume mixing ratio is instantly and uniformly doubled from 367 ppm (the year-2000 value) to 734 ppm and then maintained at the doubled level. This is a conventional doubling CO_2 experiment.
3. CO2toa: like CO2x2 but nonuniform CO_2 perturbations are prescribed so that the spatial distribution of the TOA forcing is homogenized. The CO_2 prescription is explained in detail in the following section.
4. CO2sfc: like CO2toa but different CO_2 perturbations are prescribed so that the surface forcing is homogenized.
5. CO2atm: like CO2toa but different CO_2 perturbations are prescribed so that the atmospheric forcing is homogenized.

All the experiments are initialized from the same initial atmospheric and oceanic states and then integrated for 50 years. We then analyze the changes in the TOA, surface, and atmospheric energy fluxes, defined as the mean of last 10 model years in each forcing experiment minus the mean of the corresponding years in the CONTROL experiment. Note that as indicated by the magnitudes of global mean surface warming as well as the energy imbalances in Table 1, the model approaches but does not reach equilibrium yet by the end of the simulation. However, the use of transient climate change simulations is not uncommon in the PET analyses [e.g., *Hwang and Frierson*, 2010; *Zelinka and Hartmann*, 2012] and should not affect our conclusions because (1) the forcing that we are most concerned with in this study is instantaneous forcing which does not depend on climate evolution and (2) we found in previous work [*Zhang and Huang*, 2014; *Huang et al*., 2016b] that the feedbacks analyzed from transient climate change do not qualitatively differ from those analyzed from equilibrium climate change (see further discussions in section 2.4). In addition, the subtraction of same model years of the CONTROL experiment suppresses the impacts of climatological radiation imbalance and possible climate drift in the CESM integration (assuming that the drift and imbalance do not differ between the experiments).

2.2. Forcing

We use the rapid radiative transfer model (RRTM) [*Mlawer et al*., 1997] for quantifying the instantaneous CO_2 forcing. To calculate the forcing in the CO2x2 experiment, the radiative fluxes at CO_2 concentrations of year-

Table 1. Global Mean Instantaneous Radiative Forcing, Overall Feedback, and Surface Temperature Responses in the Forcing Experiments

	Forcing (W m^{-2})			Feedback (W m^{-2})			Surface
	TOA	SFC	ATM	TOA	SFC	ATM	Temperature (K)
CO2x2	2.6	1.4	1.2	−1.4	−0.2	−1.1	2.0
CO2toa	2.5	1.6	1.0	−0.9	−0.1	−0.8	2.4
CO2sfc	3.5	1.5	2.0	−2.1	−0.2	−1.9	2.3
CO2atm	1.8	0.8	1.0	−1.2	−0.2	−1.0	1.4

2000 (367 ppm) and the doubled value CO_2 (734 ppm) are calculated off-line from 6-hourly atmospheric profiles from the CONTROL experiment at every model grid box for 5 years. We then calculate the instantaneous CO_2 forcing as the 5 year mean difference between the two sets of radiative fluxes. The forcing is calculated at TOA and surface (SFC), respectively. The radiative fluxes are defined downward positive in all cases. The difference between the TOA and SFC forcings (TOA minus SFC) renders the atmospheric (ATM) forcing. In all the cases, positive values mean warming effect.

The global mean instantaneous forcing in the CO2x2 experiment is 2.6 W m^{-2} at the TOA, 1.4 W m^{-2} at the surface, and 1.2 W m^{-2} for the atmosphere. As shown in Figure 1, although the atmospheric CO_2 concentration is uniformly changed in the CO2x2 experiment, its radiative forcing still depends on background atmospheric conditions and thus varies geographically [*Zhang and Huang*, 2014; *Merlis*, 2015; *Huang et al*., 2016a]. The zonal mean TOA forcing value generally decreases from low to high latitudes following the meridional gradient of the surface temperature. In contrast, the zonal mean surface forcing has a minimum at the equator because the strong and spectrally overlapping absorption of water vapor and cloud in the tropical

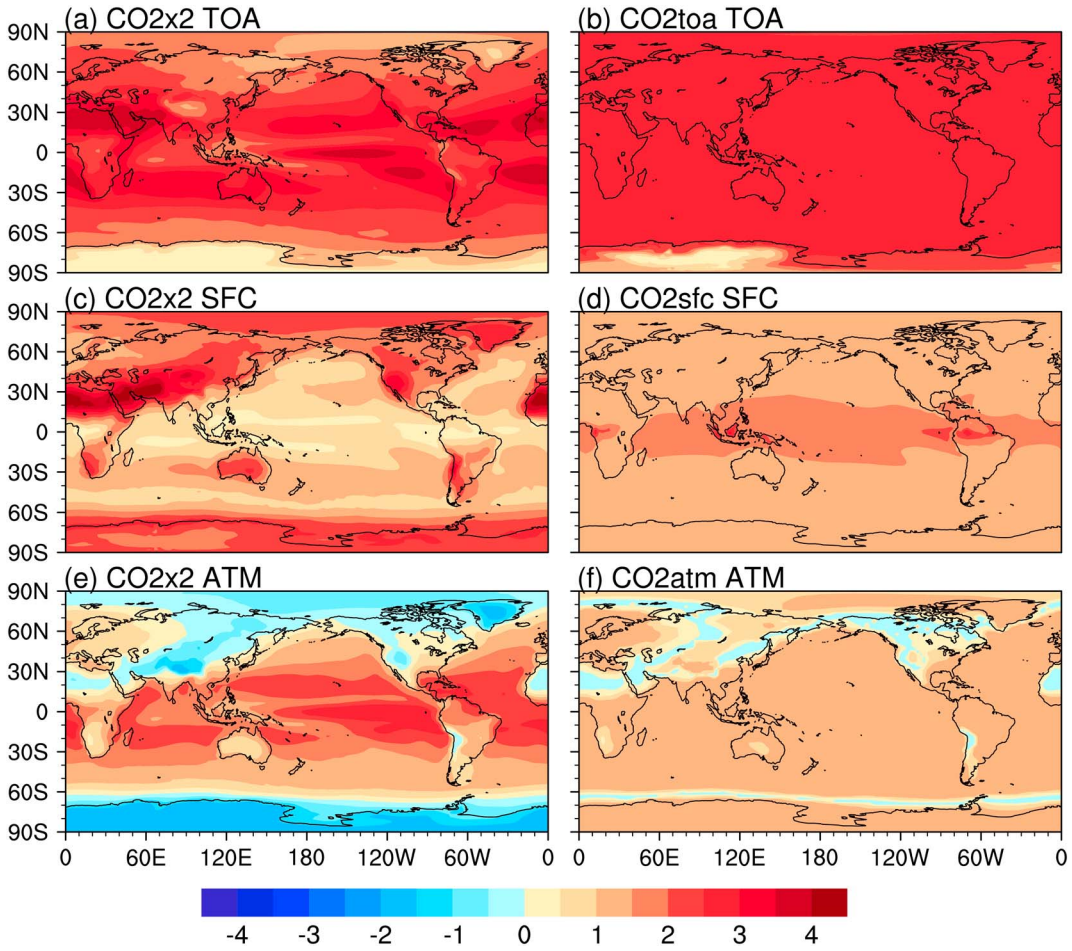

Figure 1. RRTM-calculated instantaneous radiative forcing in the GCM experiments. The panels in the three rows are the TOA, surface (SFC), and atmospheric (ATM) forcings in order, in the units of W m^{-2}. (a, c, and e) The forcing in the CO2x2 experiment. (b, d, and f) The homogenized TOA, SFC, and ATM forcings in the CO2toa, CO2sfc, and CO2atm experiments, respectively.

atmosphere makes the downwelling infrared radiation insensitive to the CO_2 perturbation. As a result, the atmospheric forcing is positive at low latitudes and negative at high latitudes.

In the CO2toa experiment, nonuniform CO_2 perturbations are prescribed so that the TOA forcing pattern is homogenized (see Figure 1). In order to achieve this, we take advantage of the logarithmic dependency of the CO_2 forcing on CO_2 concentration [*Huang and Bani Shahabadir*, 2014] and inversely determine the CO_2 concentration values in every grid box from the local forcing calculated in the CO2x2 experiment:

$$p_2 = p_1 \cdot 2^{(F_0/F)} \tag{1}$$

where p^1 is the CO_2 volume mixing ratio in the CONTROL experiment, 367 ppm; F_0 is the global mean forcing, 2.6 W m^{-2}; and F is the local forcing at each grid box in the CO2x2 experiment. The CO_2 concentrations in the CO2toa experiment are prescribed according to equation (1), except in the Antarctica where the local forcing of doubling CO_2 is so weak that it would require more than 1000 times CO_2 increase to reach forcing magnitude F_0. Such high CO_2 concentrations would be unrealistic and beyond the valid range of current radiation codes. So we have limited our CO_2 perturbations to be within 300 times of the original value (about 10% of air mass maximum).

The CO_2 concentrations in the CO2sfc and CO2atm experiments are prescribed similarly following equation (1), although the forcing values used in the equation are surface and atmospheric forcing, respectively, instead. Figure 1 shows the RRTM-calculated 5 year mean forcing patterns in these experiments. As shown by these accurately computed forcing distributions, as well as the global mean values summarized in Table 1, the targeted forcing (TOA, SFC, or ATM forcings, respectively) is greatly homogenized in each homogenization experiment. Although there remain regions where the forcing values differ due to the restriction of CO_2 perturbation as described above, the meridional gradients of the targeted forcing are largely eliminated in every experiment. Comparisons between the CO2x2 experiment and these homogenization experiments allow us to identify the climate responses related to the nonuniform patterns of the CO_2 forcing. We note that the forcing homogenization here is achieved through varying atmospheric CO_2 concentration and thus faithfully retains all the radiative impacts of the forcing agent (CO_2) that are consistent with the targeted flux changes at TOA, SFC, or ATM. This is different from previous idealized experiments that add a "ghost" flux or SST perturbations that are spatially uniform or nonuniform [e.g., *Alexeev et al*., 2005; *Hill et al*., 2015; *Marshall et al*., 2014].

2.3. Feedback

The initial radiative perturbation caused by CO_2 leads to complex changes in atmospheric and surface variables, which in turn lead to further changes in radiation fluxes at both TOA and surface, as well as changes in latent heat (LH) and sensible heat (SH) fluxes at the surface. Here we term these subsequent energy flux changes caused by the variables other than the forcing agent (CO_2) *feedback*. We do not distinguish between rapid and slow atmospheric responses [*Sherwood*, 2015] and quantify their overall radiative effect as feedback. We conduct our analysis this way because we are mainly interested in whether or not the PET change is controlled by instantaneous forcing, which is equally subject to the complications of rapid and slow responses. Moreover, previous research showed that accounting for forcing adjustments (the rapid responses) does not improve the predictability of PET change [*Huang et al*., 2016a].

We measure radiative feedback by using a radiative kernel method [*Soden et al*., 2008; *Shell et al*., 2008]. In this method, we measure a noncloud radiative feedback as

$$\Delta R_X = \frac{\partial R}{\partial X}\Delta X \tag{2}$$

Here R represents longwave (LW) or shortwave (SW) radiation fluxes at either TOA or surface in every model grid box. The $\frac{\partial R}{\partial X}$ is a radiative sensitivity kernel, which has been precalculated for each calendar month for surface and atmospheric temperature (T), atmospheric water vapor (WV), and surface albedo (A). The ΔX is the 10 year monthly mean change in each of these variables from CONTROL to each forcing experiment (see section 2.1).

In order to measure the feedback impacts on atmospheric energy budget, we have developed a new set of kernels of, not only TOA, but also surface radiation fluxes. These kernels are calculated using RRTM and global

atmospheric profiles from the ERA-Interim reanalysis data set [*Dee et al*., 2011]. These profiles are at 2.5° × 2.5° spatial resolution and 6-hourly temporal resolution and are of 5 years: 2008–2012. For each profile, clear- and all-sky radiative fluxes are calculated for multiple times: first with the original profile and then with one variable being perturbed at a time. The perturbations are applied to surface temperature (+1 K), atmospheric temperature at 19 vertical layers (+1 K), atmospheric specific humidity at 19 vertical layers (with increment needed to maintain the relative humidity unchanged when temperature increases by 1 K), and surface albedo (+0.01), respectively. If ΔR_j denotes the radiative change due to each perturbation ΔX_i (i indexes different vertical levels) applied to the jth profile, the instantaneous radiative sensitivity to X_i is $\left(\frac{\partial R}{\partial X_i}\right)_j = \frac{\Delta R_j}{\Delta X_i}$. Monthly mean kernels of each calendar month at every grid box are then averaged from all the instantaneous sensitivities of that month of the 5 years: $\frac{\partial R}{\partial X_i} = \frac{1}{n}\sum_{j=1}^{n}\left(\frac{\partial R}{\partial X_i}\right)_j$, where n is about 600, i.e., 4 times daily × 30 days per month × 5 months (same calendar months of 2008–2012). The kernels are calculated for LW and SW radiation fluxes at TOA and surface, respectively, with all the fluxes defined to be downward positive. The difference between TOA and surface flux kernels renders the atmospheric radiation kernels, which measure the convergence (if positive) of radiation flux in the atmospheric column due to each perturbation. Although the kernels are computed from reanalysis atmosphere, when applying them in the GCM feedback analysis, we find that using the kernels we can well reproduce GCM-simulated radiation anomaly (the radiation closure generally reaches >90% in terms of global mean clear-sky anomaly; see Figures S1 and S2 in the supporting information) and thus affirms the appropriateness of applying these kernels to analyzing the feedback in the GCMs.

Figure 2 illustrates the all-sky zonal and annual mean patterns of the atmospheric radiation kernels. When atmospheric temperature increases, the atmosphere radiates more energy (due to Planck's law) to space and to the Earth surface (which means energy loss at a higher rate for the atmosphere); hence, the temperature kernels are generally negative. In contrast, the water vapor kernels can be either positive or negative depending on where the humidity increment occurs. When the water vapor content increases, both the atmospheric thermal emission and its absorption of the surface emission increase. Moistening of the lower troposphere or stratosphere cools the atmosphere because the former effect dominates, while moistening of the middle and upper troposphere warms the atmosphere because the latter effect dominates. Additional illustrations of our kernels and comparison to those of others [*Shell et al*., 2008; *Soden et al*., 2008] are shown in Figures S3–S9.

The cloud radiative feedback is then measured as

$$\Delta R_C = \Delta \mathrm{R} - F - \sum \Delta R_X \tag{3}$$

Here ΔR is the CESM-calculated radiation change, F is the RRTM-calculated instantaneous forcing, $\sum \Delta R_X$ is the sum of all the noncloud radiative feedback calculated using the kernel method.

In order to intercompare the feedback in experiments of different forcing and warming magnitudes, we calculate the feedback parameters (units: W m^{-2} K^{-1}) by normalizing the feedback in each experiment with the global mean surface temperature change:

$$\lambda_X = \frac{\Delta R_X}{\langle \Delta T_s \rangle} \tag{4}$$

2.4. PET

As the local energy budgets of the atmosphere and ocean need to be rebalanced during global warming, a change in the vertical energy flux at the atmospheric or oceanic boundaries implies an offsetting change in horizontal energy transport. In an equilibrium climate, we can calculate the overall (atmospheric plus oceanic) PET as

$$\mathrm{PET}(\phi) = 2\pi a^2 \int_{\pi}^{\phi} R(\phi') \cos\phi' \, d\phi' \tag{5}$$

Here PET(ϕ) is the northward energy flux across a latitude ϕ, a is the radius of the Earth, and $R(\phi)$ is the zonal mean TOA net radiation anomaly (with respect to the global mean) at latitude ϕ relevant to the global mean.

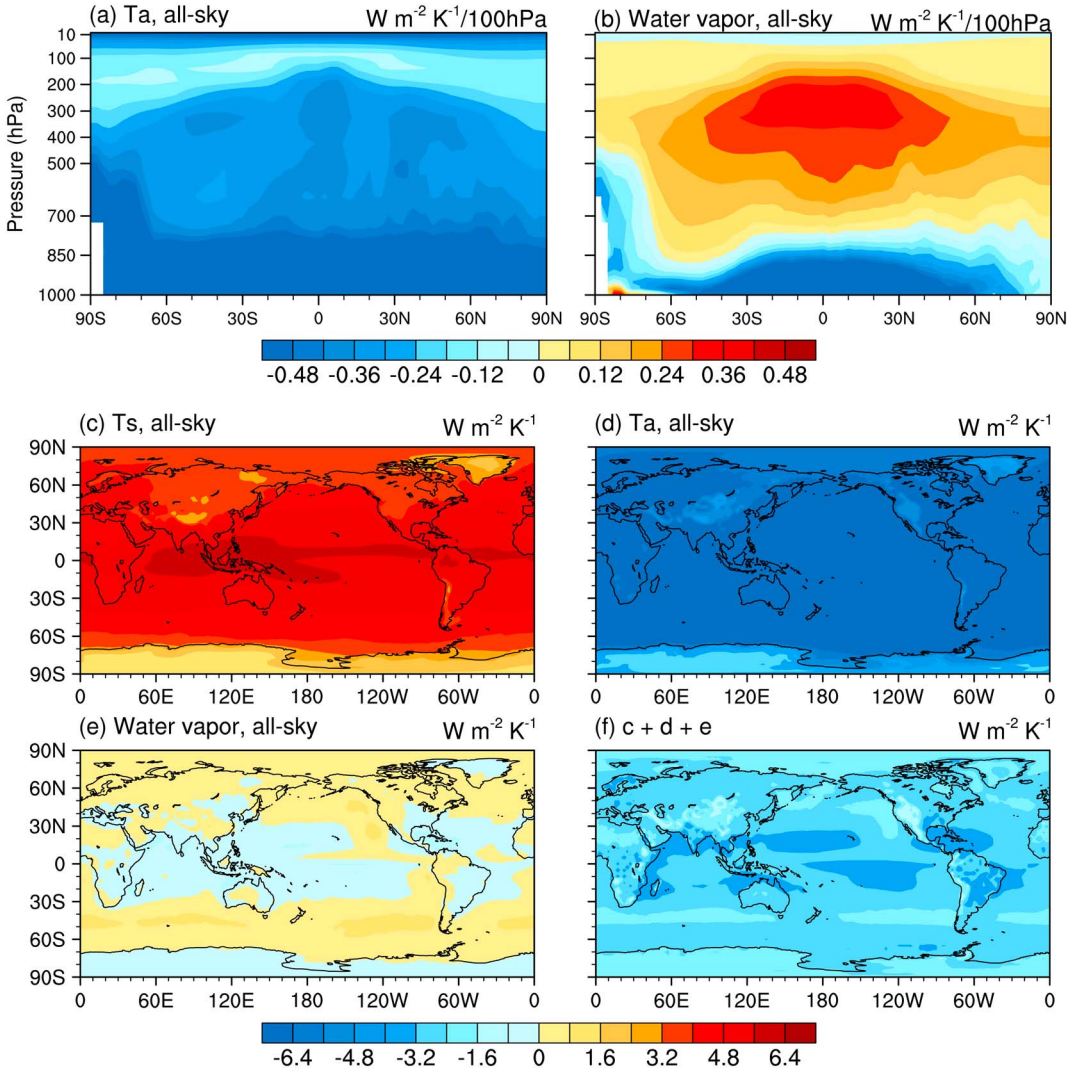

Figure 2. All-sky atmospheric radiation kernels. (a and b) Zonal and annual mean atmospheric temperature and water vapor kernel, units: W m^{-2} K^{-1}/100 hPa. They quantify the net (LW + SW) atmospheric radiation change due to +1 K temperature change in every 100 hPa thick atmospheric layer and that due to the humidity change that maintains relative humidity when temperature increases by 1 K in every 100 hPa thick atmospheric layer, respectively.(c–e) Geographic distributions of annual mean surface temperature, vertically integrated atmospheric temperature, and vertically integrated water vapor kernels, units: W m^{-2} K^{-1}. (f) The sum of Figures 2c–2e, which represents the atmospheric radiation change when the surface and atmosphere uniformly warm by 1 K while conserving relative humidity.

Based on this equation, the change in PET from the control climate to the perturbed climate, $\Delta PET(\phi)$, can be integrated from the change in net vertical flux, $\Delta R(\phi)$. Using the partial contributions to the changes in the TOA, SFC, and ATM energy budgets diagnosed using the methods outlined above, we can then infer the changes in the overall, atmospheric, and oceanic PETs, respectively, due to forcing and different feedbacks. Note that the global mean of the forcing or feedback is removed when calculating the PET due to each of them. Positive values determined from equation (5) indicate northward PET anomalies, i.e., strengthening of PET if in the Northern Hemisphere but weakening of it in the Southern Hemisphere.

Although only 50 year nonequilibrium (especially with respect to ocean) simulations are used in our diagnosis, longer integrations available elsewhere (Figure S10) show that the PET inferred from 50 year simulations closely resemble the long-term (equilibrium) responses, despite some differences. For instance, the oceanic PET is more northward in the 41–50 year period than in the 141–150 year period in the Southern Hemisphere in nearly every model, which likely relates to delayed Southern Ocean warming. In addition, very interestingly, the oceanic PETs inferred from surface energy fluxes approximate the PETs explicitly simulated by

the CESM (Figure S11). Although regional differences exist between them, e.g., the sign in the latitudes from 10°N to 60°N (Figure S11c), the overall pattern of the PET response to CO_2 and the difference between the homogeneous and inhomogeneous forcing experiments are captured by the inference based on equation (5). These results justify the discussions based on the inferred PET changes in the following.

3. Results

3.1. CO2x2 Experiment

Figure 3 shows the zonal mean radiative forcing and feedback parameters in the CO2x2 experiment, as well as the nonradiative LH and SH feedback. Note that both forcing and feedback are normalized by the global mean surface temperature change (thus in the units of W m^{-2} K^{-1}) in order to facilitate intercomparison between them across different experiments. Also shown here are the forcing and feedback in 10 GCMs from the CMIP5 abrupt 4xCO2 experiment, analyzed using the method of *Zhang and Huang* [2014]. In this method, the global distribution of feedback, as well as forcing (a novelty of the method), is diagnosed using the radiative kernel method. The last 10 years of the 150 year GCM simulations are used for the analysis.

Figure 4 shows the PET changes inferred, according to equation (5), from the partial energy flux changes shown in Figure 3.

Although the forcing magnitudes are different (by a factor of 2), Figures 3 and 4 show that the normalized feedback patterns are remarkably similar between the doubling and quadrupling experiments and between different GCMs, indicating that these feedbacks are insensitive to the magnitude of forcing (and thus warming) given the same forcing pattern. These prominent results are worth noting:

1. The CO_2 forcing is positive at both TOA and surface because of its greenhouse effect—CO_2 decreases the outgoing radiation from the surface and atmosphere to space but increases the downwelling thermal radiation from the atmosphere to the surface. However, the TOA forcing generally decreases from equator to pole and has a strong meridional gradient, while the surface forcing has a weaker and opposite meridional gradient. This is because the high water vapor concentration in the tropical lower troposphere makes the atmospheric absorptivity there already very large and thus insensitive to the CO_2 perturbation, which limits the effect of CO_2 on the downwelling radiation. This renders interesting zonal mean patterns of atmospheric forcing, which is positive in the low latitudes and negative in the high latitudes (see Figures 1 and 3).

The nonuniform zonal mean patterns of the forcing have strong implications for the PET changes. The forcing distribution by itself requires significant strengthening of the atmospheric PET, weakening of the oceanic PET, and strengthening of the overall (atmosphere plus ocean) PET (see Figure 4).

2. The water vapor feedback is also positive at TOA and SFC because of a similar greenhouse effect. However, different from the CO_2 forcing, the feedback at both TOA and surface peaks in the tropics and decreases with latitude, which renders a rather flat zonal mean atmospheric feedback pattern (see Figure 3). These zonal mean patterns mean that the water vapor radiative feedback drives an enhancement of oceanic PET but has little effect on the atmospheric PET (see Figure 4). This result contradicts the statement that water vapor radiative feedback is a major cause of the atmospheric PET enhancement [e.g., *Zelinka and Hartmann*, 2012], which was based on TOA-only analysis.
3. The temperature feedback at TOA is negative (cooling effect) because the Planck function demands higher energy loss rate at warmer temperatures. At the surface, there is a competition between increase in upwelling radiation due to surface warming and increase in downwelling radiation due to atmospheric warming, which largely offset and lead to weak negative SFC temperature feedback except in the polar regions (there the atmospheric emissivity is low so that the upwelling surface radiation prevails over downwelling atmospheric radiation [*Boé et al*., 2009; *Lesins et al*., 2012]). As a result, the atmospheric temperature feedback is also negative and peaks at the equator (see Figure 3). This drives a strong weakening of the atmospheric PET (see Figure 4), acting against the CO_2 forcing, as inferred by *Huang and Zhang* [2014].
4. The surface albedo feedback is positive and occurs in high latitudes only, which results in a strong equator-to-pole gradient in TOA and surface radiative flux changes. However, due to minimal atmospheric absorption of SW radiation, this feedback has little impact on the atmospheric energy budget or PET.

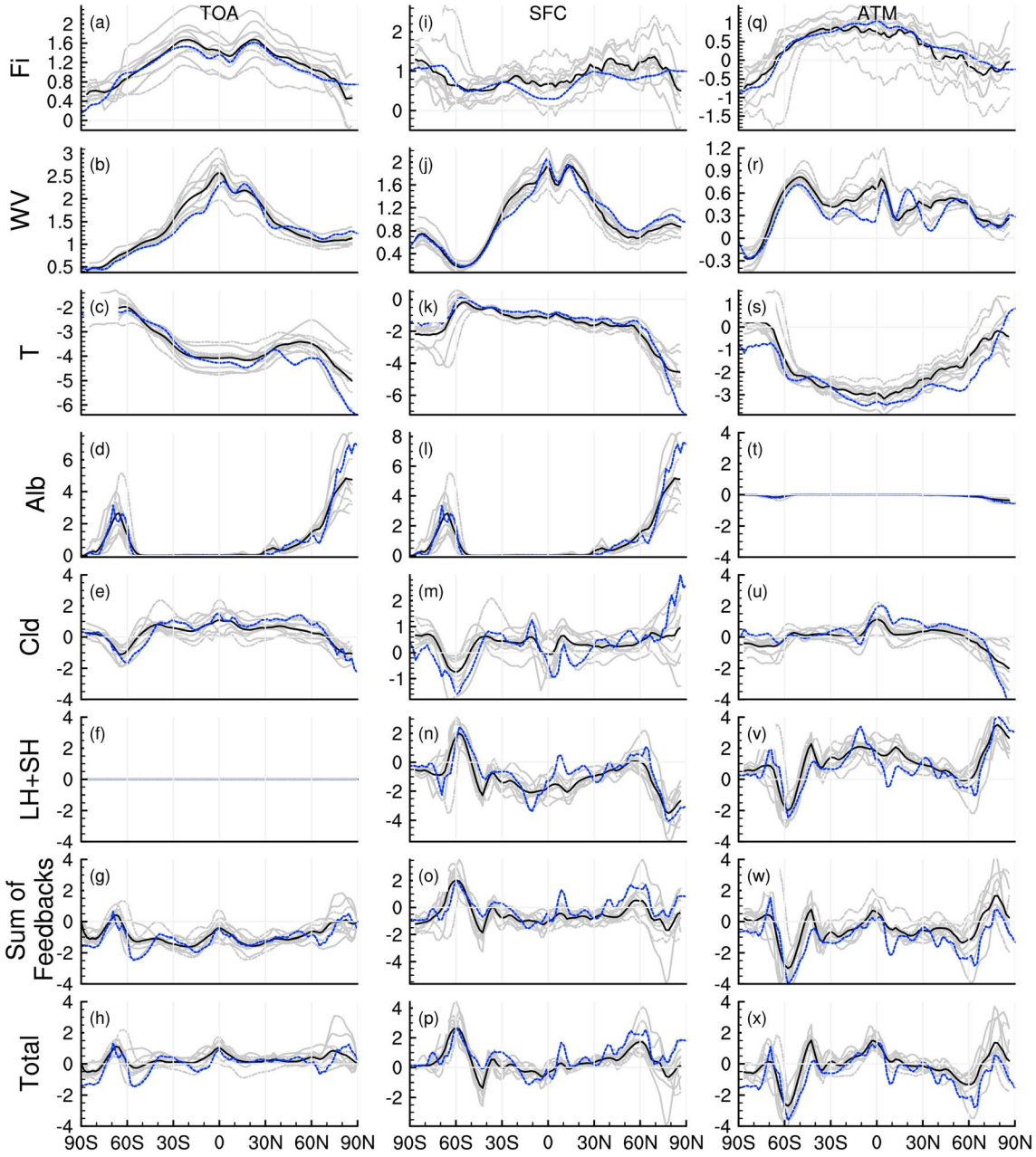

Figure 3. Zonal mean TOA, SFC, and ATM energy flux changes, normalized by global mean surface temperature change. Units: W m^{-2} K^{-1}. Shown in different rows are the changes due to CO_2 instantaneous forcing (Fi), radiative feedback of water vapor (WV), surface and atmospheric temperature (*T*), surface albedo (Alb), clouds (Cld), latent and sensible heat fluxes (LH + SH), and the sums of the components. The results from the CESM CO2x2 experiment are shown in blue; the results from CMIP5 abrupt4xCO2 experiment are shown in grey (individual GCMs) and black (ensemble mean). Note that the *y* axis ranges are not all the same, even within each row (same in the following figures).

5. The cloud feedback has more complex spatial (zonal mean) structures. The TOA cloud feedback is consistently negative at around −60° (Southern Oceans) and the North Pole. The surface feedback shows an increasing trend from the Southern Hemisphere to the Northern Hemisphere. The atmospheric feedback largely follows the TOA feedback. As cloud feedback differs substantially across the models [*Zelinka and Hartmann*, 2012; *Vial et al*., 2013; *Huang and Zhang*, 2014], the cloud effect on PET is also very uncertain, although a strengthening effect on the atmospheric PET is discernable in the results here (see Figure 4).
6. The nonradiative feedback of LH and SH also have complex zonal mean structures. The LH flux from surface to atmosphere generally increases over ocean but decreases over land in the CESM CO2x2 experiment; the SH feedback is generally anticorrelated with the LH feedback [*Berg et al*., 2014]. This means that

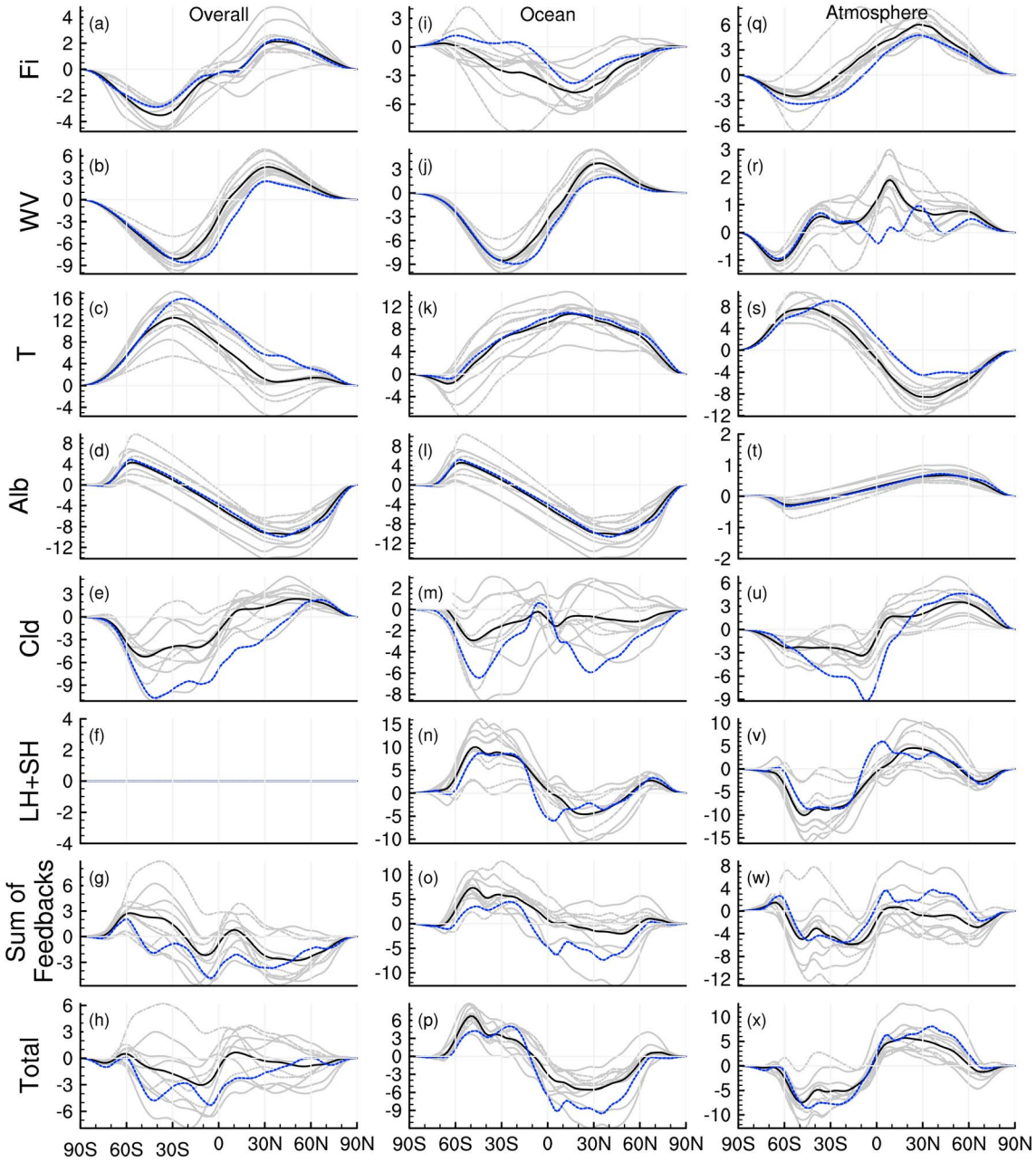

Figure 4. Overall, oceanic, and atmospheric PET changes inferred from the energy flux changes shown in Figure 3. Units: 10^{13} W K^{-1}. Note that the PET values in the control climate are in the order of 10^{15} W and the PET changes here are in the order of a few percent.

the magnitude and sign of the zonal mean LH + SH feedback result from compensations of these changes of different signs and are subject to uncertainty, which is manifested by the large inter-GCM spread of this feedback. We also notice that the LH feedback at SFC is anticorrelated with the net radiation feedback as reported by *Zelinka and Hartmann* [2012]. The LH + SH feedback induces strengthening of atmospheric PET and weakening of the oceanic PET, although, like cloud feedback, this result is subject to large uncertainty (intermodel discrepancies).

7. The overall effect of the above forcing and feedback components is a robust weakening of the oceanic PET and strengthening of the atmospheric PET. Due to their compensation, the sign of the overall PET change is rather uncertain (see Figure 4). It is interesting to note that both atmospheric PET enhancement and oceanic PET weakening are consistent with the effects of CO_2 forcing, which suggests that the climate system evolves toward the direction driven by the initial forcing in spite of the complex feedback effects.

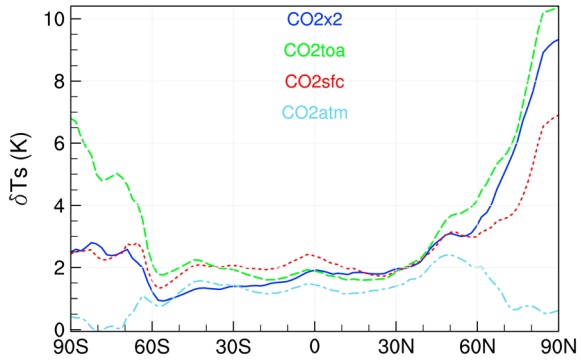

Figure 5. Zonal mean surface temperature changes in the forcing experiments.

3.2. Homogenization Experiments

The analysis above separates the radiative effects of radiative forcing and individual feedback and verifies that the inhomogeneous distribution (meridional gradient) of CO_2 forcing accounts for atmospheric PET strengthening and oceanic PET weakening. However, this analysis is built upon the assumption that the feedback is independent of forcing and their effects can be linearly separated. It is not clear whether the feedback depends on CO_2 forcing pattern and how much of the PET changes may be attributed to such possible dependency (a nonlinear effect, e.g., the terms concerning $\Delta X_1 \Delta X_2$ in a Taylor expansion of the PET perturbation, where X_1 and X_2 are forcing and feedback, respectively). We address these questions by conducting a set of homogenization experiments: CO2toa, CO2sfc, and CO2atm, in which the TOA, surface, and atmospheric forcings are homogenized, respectively, using the method described in section 2.2. The differences in climate responses between the CO2x2 experiment and each of these experiments can be attributed to the forcing distribution effect.

Figure 5 shows the zonal mean surface temperature responses in all the forcing experiments. The warming patterns are similar in the CO2x2, CO2toa, and CO2sfc experiments except for a noticeably stronger warming in the Antarctica in the CO2toa experiment, which is related to the large increase in atmospheric CO_2 concentration prescribed in this region. The warming pattern in the CO2atm experiment is surprisingly different in that there is no amplification of warming in the high latitudes. This is because the CO_2 concentration in these regions is reduced in this experiment to reverse the sign of the atmospheric forcing there (see Figure 1). The results here suggest that the temperature pattern of global warming is dependent on forcing distribution, in contrast to the finding of *Xie et al*. [2013]. Interestingly, we find that the global mean surface temperature change is most correlated with surface forcing in these experiments (a correlation coefficient of 0.98; see the forcing and temperature values in Table 1), which suggests that the surface warming magnitude is mostly controlled by surface energy budget when the forcing pattern varies.

In the analysis below, we compare the zonal mean distributions of the forcing and feedback in the homogenization experiments to those in the CO2x2 experiment and focus on the energy budget (TOA, SFC, or ATM) targeted in each homogenization experiment (see the first column in Figures 6–8). We also analyze the PET changes due to the forcing and feedback differences between the CO2x2 and each homogenization experiments (the second column in Figures 6–8), calculated following equation (5), which provide a measure of the nonlinear effect of forcing inhomogeneity.

1. CO2toa experiment

Figure 6 compares the distributions of the TOA radiative forcing and feedback in the CO2x2 and CO2toa experiments, as well as the changes in the overall (atmospheric plus oceanic) PET due to their differences (CO2x2 minus CO2toa, same for the other two homogenization experiments). Figure 6n shows the PET change due to the overall effect of the forcing inhomogeneity, including the forcing distribution itself and feedback difference attributable to the forcing inhomogeneity (the nonlinear effect).

The feedback patterns in the CO2toa experiment generally resemble those in the CO2x2 experiment, although differences exist, including less strong water vapor and temperature feedback in the tropics, which largely compensate, and stronger cloud feedback in the high latitudes in both hemispheres. The overall forcing inhomogeneity effect drives a strong enhancement of the overall PET in both hemispheres (see Figure 6n). This experiment affirms a strong effect of TOA instantaneous forcing on the overall PET in that the overall PET change after considering the nonlinear forcing-feedback effects still generally follows, and is amplified from, the enhancement driven by the instantaneous forcing pattern (Figure 6h).

2. CO2sfc experiment

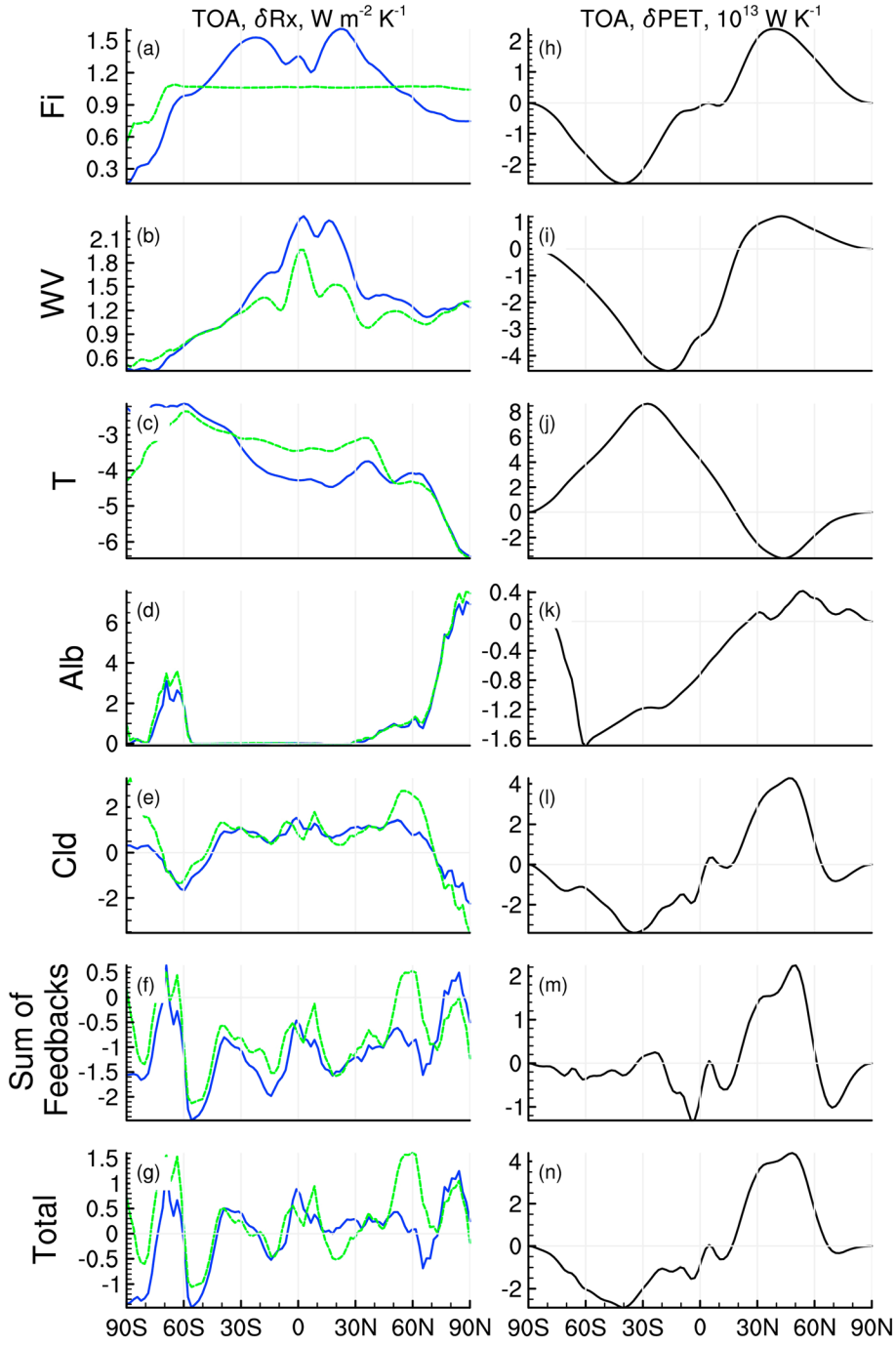

Figure 6. (a–g) Normalized zonal mean TOA forcing and feedback in the CO2x2 (blue) and CO2toa (green) experiments (units: W m^{-2} K^{-1}) and (h–n) the PET changes implied by their differences (units: 10^{13} W K^{-1}).

Figure 7 shows the distributions of the surface forcing and feedback in the CO2x2 and CO2sfc experiments and the oceanic PET changes attributable to their differences. The oceanic PET weakens but to a lesser extent in the CO2sfc experiment than in the CO2x2 experiment (which is consistent with earlier studies with idealized uniform fluxes [e.g., *Alexeev et al.*, 2005; *Marshall et al.*, 2014]), so that the overall homogeneity effect is weakening of the oceanic PET (Figure 7p). Figures 7b–7g show that the feedback patterns in the CO2sfc experiment are similar to those in the CO2x2 experiment. This means that although quantitative differences exist, the effects of all the feedback that are associated with the forcing inhomogeneity largely compensate

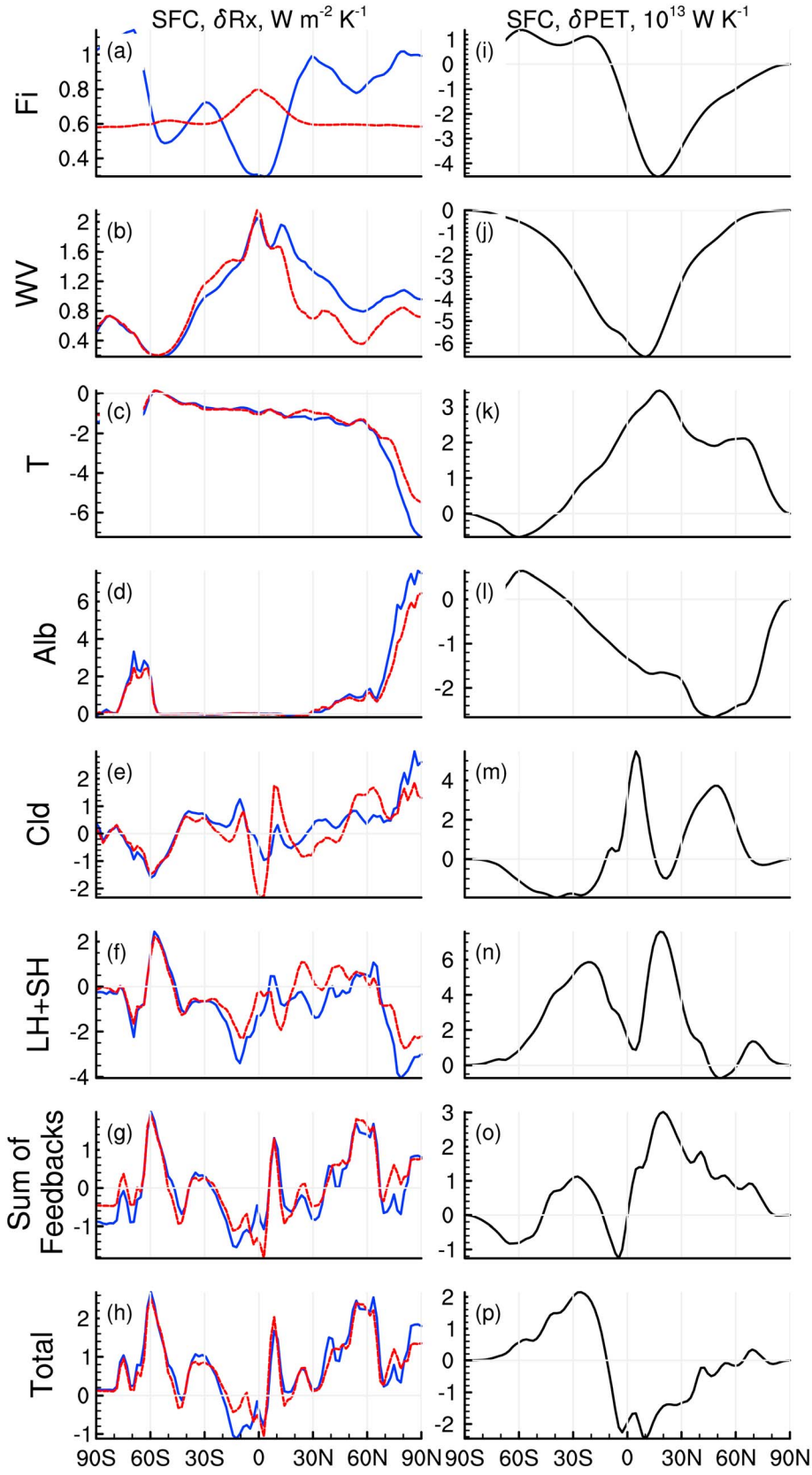

Figure 7. (a–h) Normalized zonal mean surface forcing and feedback in the CO2x2 (blue) and CO2sfc (red) experiments (units: W m^{-2} K^{-1}) and (i–p) the oceanic PET changes implied by their differences (units: 10^{13} W K^{-1}).

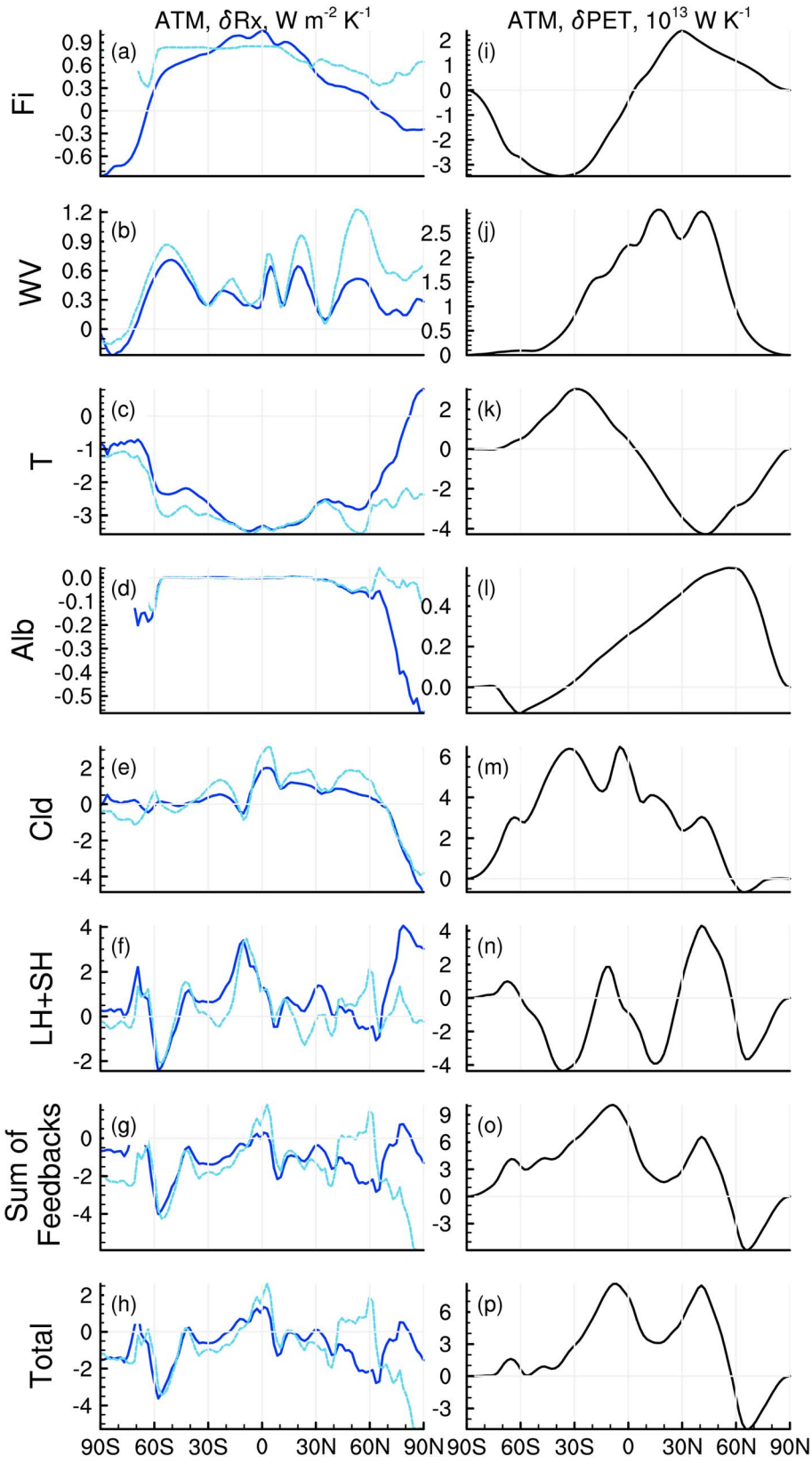

Figure 8. (a–h) Normalized zonal mean atmospheric forcing and feedback in the CO2x2 (blue) and CO2atm (cyan) experiments (units: W m^{-2} K^{-1}) and (i–p) the atmospheric PET changes implied by their differences (units: 10^{13} W K^{-1}).

(Figure 7o). Hence, this experiment affirms that the inhomogeneity effect (including the nonlinear effect between forcing and feedback) of CO_2 forcing is to drive a weakening of the oceanic PET.

3. CO2atm experiment

Figure 8 shows the distributions of the atmospheric forcing and feedback in the CO2x2 and CO2atm experiments and the atmospheric PET changes attributable to their differences. Due to the lack of warming in the high latitudes in the CO2atm experiment, the water vapor and temperature feedback differ noticeably. It was seen that the relatively stronger warming in the high latitudes (Arctic amplification) in the CO2x2 experiment drives a strong weakening of the atmospheric PET (Figure 4s) and this effect offsets the effect of atmospheric forcing inhomogeneity (Figure 4q). The results here suggest that the Arctic amplification and its effect on PET are related to forcing distribution—different forcing pattern may lead to different warming pattern, which in turn results in different overall feedback [*Armour et al*., 2013] and consequently different impact on PET. The interesting connection between Arctic amplification (temperature feedback) and CO_2 forcing pattern discovered here warrants future investigations.

The nonradiative (LH + SH) feedback associated with forcing inhomogeneity (Figure 8n) is to weaken the atmospheric PET within the tropics, which is consistent with a forcing inhomogeneity-driven weakening of tropical circulation [*Merlis*, 2015; *Xia and Huang*, 2017].

4. Conclusions and Discussions

In this study, we conduct a set of radiative forcing experiments using an atmosphere-ocean coupled GCM, CESM, and analyze the radiative forcing and feedback distributions in these experiments and their effects on atmospheric and oceanic poleward energy transports. We find that the spatial pattern of CO_2 instantaneous forcing at TOA generally decreases in magnitude from equator to pole, and this is not countered by feedback, such that the total PET is increased during global warming. Conversely, the CO_2 surface forcing increases in magnitude from equator to pole, and this is also not countered by feedback, such that the oceanic PET is reduced. It can also be inferred from the TOA and surface energy fluxes that the increase of atmospheric PET is directly driven by the CO_2 forcing pattern. Key strengths of this study include accurate quantification of instantaneous forcing using a radiative transfer model, RRTM, and separate quantification of the radiative feedback on atmospheric and oceanic energy budgets by using a new set of radiative kernels that we have developed.

As the local energy budgets of the atmosphere and ocean need to be rebalanced during global warming, zonal mean changes in the vertical energy flux at the atmospheric and oceanic boundaries require offsetting changes in the meridional energy transports. Using this constraint, we infer and compare the effects of radiative forcing and various climate feedbacks on PET in four global warming experiments:

1. CO2x2: a conventional global warming experiment in which atmospheric CO_2 concentration is uniformly doubled although its forcing pattern is inhomogeneous.
2. CO2toa: the TOA forcing pattern is homogenized.
3. CO2sfc: the surface forcing pattern is homogenized.
4. CO2atm: the atmospheric forcing pattern is homogenized.

The method used to homogenize CO_2 forcing distribution takes advantage of the well understood logarithmic dependency of the forcing (equation (1)). As shown by the results here (Figure 1), using this method we can very well homogenize the TOA, surface, and atmospheric forcings. This provides a convenient way of controlling the radiative forcing in GCM experiments.

The CO2x2 experiment conducted with CESM reproduces the robust PET changes during global warming, including enhancement of the atmospheric PET and weakening of the oceanic PET, as simulated by the CMIP5 GCMs. The partitioning of the forcing and feedback effects on PET affirms that the forcing pattern directly accounts for the PET strengthening in the atmosphere and weakening in the ocean (see Figures 3 and 4). The homogenization experiments provide additional insights on how the forcing inhomogeneity drives the PETs to change. In particular, the feedback patterns, and their impacts on PETs, associated with forcing inhomogeneity (a nonlinear effect due to the coupling between forcing and feedback) are identified (see Figures 6–8).

The results here suggest that the atmospheric and oceanic PET changes during global warming directly result from the spatial patterns of the CO_2 radiative forcing. This corroborates the earlier finding that much of the PET response discrepancies among the CMIP5 models are attributable to their differences in CO_2 forcing [*Huang et al*., 2016a].

Using a new set of radiative kernels, we also identify the key feedbacks that corroborate with forcing and reinforce the atmospheric PET enhancement and oceanic PET weakening, such as the albedo feedback in the case of oceanic PET and the cloud feedback in the case of atmospheric PET (see Figure 4), as well as the feedbacks that strongly offset the forcing effect, such as the temperature feedback in the case of atmospheric PET. Interestingly, the overall feedback effect is to reinforce the atmospheric PET enhancement and oceanic PET weakening driven by the forcing (compare the last row to the first in Figure 4).

The results point to the importance of distinguishing the forcing and feedback effects on atmospheric and oceanic budgets in order to correctly determine their effects on PET. Inaccurate attributions may result from the use of TOA radiation alone to infer atmospheric PET changes, which as shown in Figure 4 may fail in many cases. For instance, the strong effects of water vapor and albedo feedback inferred from the TOA radiation changes were highlighted in previous studies [e.g., *Zelinka and Hartmann*, 2012], but their effects are mainly exerted on the oceanic, instead of atmospheric, PET. Conversely, the temperature feedback has a considerable weakening effect on the atmospheric PET, which would not be evident from the TOA radiation analysis alone. As shown in this study, a comprehensive set of TOA and surface radiative kernels are very useful in this regard.

An interesting result is that the warming amplification in the high latitudes is suppressed in the atmospheric forcing homogenization experiment (CO2atm), in which we increase the CO_2 concentration in the low latitudes but decrease it in the high latitudes. This result suggests that the warming pattern is sensitive to forcing distribution. Particularly, local surface forcing seems essential for generating the warming amplification in the high latitudes. This highlights the importance of forcing [e.g., *Rose et al*., 2014], as opposed to feedback [e.g., *Cai*, 2005], in Artic warming amplification. Further investigations are warranted to elucidate this connection between forcing pattern and warming pattern.

Acknowledgments
We thank Daniel Feldman for the help with configuring the CESM homogenization experiments. We thank Timothy Merlis, Mark Zelinka, Nadir Jeevanjee, Allison Kolly, Steve Klein, and three anonymous reviewers for helpful comments. We thank Karen Shell and Brian Soden for making their kernels available for comparison. We acknowledge the ECMWF for the ERA-Interim data (http://apps.ecmwf.int/datasets/data/interim-full-moda/) and the Atmospheric Environment Research for RRTMG model (http://rtweb.aer.com/rrtm_frame.html) used for developing the radiative kernels. The radiative kernels generated in this work can be obtained from Huang's website: http://www.meteo.mcgill.ca/~huang/. The work is supported by grants from the Discovery Program of the Natural Sciences and Engineering Council of Canada (RGPIN 418305-13) and the Team Research Project Program of the Fonds de recherché Nature et technologies of Quebec (PR-190145).

References

Alexeev, V. A., P. L. Langen, and J. R. Bates (2005), Polar amplification of surface warming on an aquaplanet in "ghost forcing" experiments without sea ice feedbacks, *Clim. Dyn.*, *24*(7–8), 655–666, doi:10.1007/s00382-005-0018-3.

Armour, K. C., C. M. Bitz, and G. H. Roe (2013), Time-varying climate sensitivity from regional feedbacks, *J. Clim.*, *26*(13), 4518–4534, doi:10.1175/JCLI-D-12-00544.1.

Bjerknes, J. (1964), *Atlantic Air-Sea Interaction. Advances in Geophysics*, vol. 10, pp. 1–82 , Academic Press, New York.

Berg, A., et al. (2014), Interannual coupling between summertime surface temperature and precipitation over land: Processes and implications for climate change, *J. Clim.*, *28*(3), 1308–1328, doi:10.1175/JCLI-D-14-00324.1.

Boé, J., A. Hall, and X. Qu (2009), Current GCMs' unrealistic negative feedback in the Arctic, *J. Clim.*, *22*(17), 4682–4695, doi:10.1175/2009JCLI2885.1.

Bryden, H., H. Longworth, and S. Cunningham (2005), Slowing of the Atlantic meridional overturning circulation at 25°N, *Nature*, *438*, 655–657, doi:10.1038/nature04385.

Cai, M. (2005), Dynamical amplification of polar warming, *Geophys. Res. Lett.*, *32*, L22710, doi:10.1029/2005GL024481.

Dee, D. P., et al. (2011), The ERA-Interim reanalysis: Configuration and performance of the data assimilation system, *Q. J. R. Meteorol. Soc.*, *137*, 553–597.

Held, I. M., and B. J. Soden (2006), Robust Responses of the Hydrological Cycle to Global Warming, *J. Clim.*, *19*, 5686–5699.

Hill, S. A., Y. Ming, and I. M. Held (2015), Mechanisms of forced tropical meridional energy flux change, *J. Clim.*, *28*(5), 1725–1742, doi:10.1175/JCLI-D-14-00165.1.

Huang, Y., and M. Bani Shahabadi (2014), Why logarithmic? A note on the dependence of radiative forcing on gas concentration, *J. Geophys. Res. Atmos.*, *119*, 13,683–13,689, doi:10.1002/2014JD022466.

Huang, Y., and M. Zhang (2014), The implication of radiative forcing and feedback for poleward energy transport, *Geophys. Res. Lett.*, *41*, 1665–1672, doi:10.1002/2013GL059079.

Huang, Y., X. Tan and Y. Xia, (2016a), Inhomogeneous radiative forcing of homogeneous greenhouse gases, *J. Geophys. Res. Atmos.*, *121*, 2780–2789, doi:10.1002/2015JD024569.

Huang, Y., M. Zhang, Y. Xia, Y. Hu, and S. Son (2016b), Is there a stratospheric radiative feedback in global warming simulations?, *Clim. Dyn.*, *46*(1–2), 177–186, doi:10.1007/s00382-015-2577-2.

Hwang, Y.-T., and D. M. W. Frierson (2010), Increasing atmospheric poleward energy transport with global warming, *Geophys. Res. Lett.*, *37*, L24807, doi:10.1029/2010GL045440.

Hurrell, J. W., et al. (2013), The Community Earth System Model: A framework for collaborative research, *Bull. Am. Meteorol. Soc.*, *94*(9), 1339–1360.

Lesins, G., T. J. Duck, and J. R. Drummond (2012), Surface energy balance framework for Arctic amplification of climate change, *J. Clim.*, *25*(23), 8277–8288, doi:10.1175/JCLI-D-11-00711.1.

Marshall, J., et al. (2014), The ocean's role in polar climate change: Asymmetric Arctic and Antarctic responses to greenhouse gas and ozone forcing, *Phil. Trans. R. Soc. A*, *372*, 20130040, doi:10.1098/rsta.2013.0040.

Merlis, T. M. (2015), Direct weakening of tropical circulations from masked CO_2 radiative forcing, *Proc. Natl. Acad. Sci.*, *112*, 13,167–13,171, doi:10.1073/pnas.1508268112.

Mlawer, E. J., S. J. Taubman, P. D. Brown, M. J. Iacono, and S. A. Clough (1997), Radiative transfer for inhomogeneous atmospheres: RRTM, a validated correlated-k model for the longwave, *J. Geophys. Res.*, *102*, 16,663–16,682.

Neale, R. B., C.-C. Chen, A. Gettelman, P. H. Lauritzen, S. Park, D. L. Williamson, A. J. Conley, R. Garcia, D. Kinnison, and J.-F. Lamarque (2010), Description of the NCAR community atmosphere model (CAM 5.0), *NCAR Tech. Note NCAR/TN-486+ STR*.

Rose, B. E. J., K. C. Armour, D. S. Battisti, N. Feldl, and D. D. B. Koll (2014), The dependence of transient climate sensitivity and radiative feedbacks on the spatial pattern of ocean heat uptake, *Geophys. Res. Lett.*, *41*, 1071–1078, doi:10.1002/2013GL058955.

Shell, K. M., J. T. Kiehl, and C. A. Shields (2008), Using the radiative kernel technique to calculate climate feedbacks in NCAR's Community Atmospheric Model, *J. Clim.*, *21*, 2269–2282.

Sherwood, S. C., S. Bony, O. Boucher, C. Bretherton, P. M. Forster, J. M. Gregory, and B. Stevens (2015), Adjustments in the forcing-feedback framework for understanding climate change, *Bull. Am. Meteorol. Soc.*, *96*, 217–228, doi:10.1175/BAMS-D-13-00167.1.

Soden, B. J., I. M. Held, R. Colman, K. M. Shell, J. T. Kiehl, and C. A. Shields (2008), Quantifying climate feedbacks using radiative kernels, *J. Clim.*, *21*, 3504–3520.

Trenberth, K., and J. Caron (2001), Estimates of meridional atmosphere and ocean heat transport, *J. Clim.*, *14*, 3433–3443.

Trossman, D. S., J. B. Palter, T. M. Merlis, Y. Huang, and Y. Xia (2016), Large-scale ocean circulation-cloud interactions alter the pace of transient climate change, *Geophys. Res. Lett.*, *43*, 3935–3943, doi:10.1002/2016GL067931.

Vial, J., J.-L. Dufresne, S. Bony (2013), On the interpretation of inter-model spread in CMIP5 climate sensitivity estimates, *Clim. Dyn.*, *41*(11–12), 3339–3362 doi:10.1007/s00382-013-1725-9.

Xia, Y., and Y. Huang (2017), Differential radiative heating drives tropical atmospheric circulation weakening, *Geophys. Res. Lett.*, *44*, doi:10.1002/2017GL075678.

Xie, S.-P., B. Lu, and B. Xiang (2013), Similar spatial patterns of climate responses to aerosol and greenhouse gas changes, *Nat. Geosci.*, *6*(10), 828–832, doi:10.1038/ngeo1931.

Zhang, M., and Y. Huang (2014), Radiative forcing of quadrupling CO_2, *J. Clim.*, doi:10.1175/JCLI-D-13-00535.

Zelinka, M. D., and D. L. Hartmann (2012), Climate Feedbacks and Their Implications for Poleward Energy Flux Changes in a Warming Climate, *J. Clim.*, *25*, 608–624.